Astronomy & Astrophysics manuscript no. M3_draft_vs2
June 13, 2019

MASCARA-3b

A hot Jupiter transiting a bright F7 star in an aligned orbit

M. Hjorth[1]⋆, S. Albrecht[1], G. J. J. Talens[2], A. B. Justesen[1], G.P.P.L. Otten[3], V. Antoci[1], P. Dorval[4], E. Foxell[5], M. Fredslund Andersen[1], F. Grundahl[1], F. Murgas[6,7], E. Palle[6,7], R. Stuik[4], I. A. G. Snellen[4], and V. Van Eylen[8]

[1] Stellar Astrophysics Centre, Department of Physics and Astronomy, Aarhus University, Ny Munkegade 120, DK-8000 Aarhus C, Denmark
[2] Institut de Recherche sur les Exoplanètes, Département de Physique, Université de Montréal, Montréal, QC H3C 3J7, Canada
[3] Aix Marseille Univ, CNRS, CNES, LAM, Marseille, France
[4] Leiden Observatory, Leiden University, Postbus 9513, 2300 RA, Leiden, The Netherlands
[5] Department of Physics, University of Warwick, Coventry CV4 AL, UK
[6] Instituto de Astrofísica de Canarias (IAC), Vía Láctea s/n, 38205, La Laguna, Tenerife, Spain
[7] Departamento de Astrofísica, Universidad de La Laguna, 38205, La Laguna, Tenerife, Spain
[8] Department of Astrophysical Sciences, Princeton University, 4 Ivy Lane, Princeton, NJ 08544, USA

Received Month Date, Year; accepted Month Date, Year

ABSTRACT

We report the discovery of MASCARA-3b, a hot Jupiter orbiting its late, bright ($V = 8.33$) F-type host every 5.55149 ± 0.00001 days on an almost circular orbit ($e = 0.085^{+0.023}_{-0.022}$). It is the fourth exoplanet discovered with the Multi-site All-Sky CAmeRA (MASCARA), and the first of these which orbits a late-type star. Follow-up spectroscopic measurements were obtained in and outside of transit with the Hertzsprung SONG telescope. Combining the MASCARA photometry and SONG radial velocities reveals a radius and mass of $1.35 \pm 0.05\ R_{\rm Jup}$ and $4.2 \pm 0.2\ M_{\rm Jup}$. In addition, SONG spectroscopic transit observations were obtained on two separate nights. From analyzing the mean out of transit broadening function we obtain $v \sin i_\star = 20.4 \pm 0.4$ km s^{-1}. In addition, investigating the Rossiter-McLaughlin effect, as observed in the distortion of the stellar lines directly, we find the projected obliquity to be $\lambda = 10.5 \pm 24.9$ deg, consistent with alignment.

Key words. Planetary systems – stars: individual: MASCARA-3

1. Introduction

With more than 4000[1] planets confirmed to date, the field of exoplanets has experienced a huge growth since its beginning two decades ago. This large number of discoveries has in particular been the product of extensive ground- and space-based transit photometry surveys, such as the missions of HAT (Bakos et al. 2004), WASP (Pollacco et al. 2006), CoRoT (Barge et al. 2008), Kepler (Borucki et al. 2010) and K2 (Howell et al. 2014). However, because of saturation limits, these surveys are prevented from monitoring the brightest stars.

Transiting planets orbiting bright stars are important since they offer follow-up opportunities not available for fainter sources, allowing for detailed characterisation of the planets atmosphere and the systems orbital architecture. This includes the detection of e.g. water in the planetary atmosphere through high-resolution transmission spectroscopy (e.g. Snellen et al. 2010) and measurements of its spin-orbit angle through observations of the Rossiter-McLaughlin (RM) effect.

From space, the brightest exoplanet host stars are currently being probed thanks to the launch of TESS (Ricker et al. 2015), while ground-based projects doing the same include KELT (Pepper et al. 2007) and the MASCARA (the Multi-Site All-sky CAmeRA) survey (Talens et al. 2017b). The latter aspires to find close-in transiting giant planets orbiting the bright stars well suited for detailed atmospheric characterisation. This has so far led to the discovery and characterisation of MASCARA-1, MASCARA-2 and MASCARA-4, three hot Jupiters orbiting A-type stars (Talens et al. 2017a, 2018b; Dorval et al. 2019).

In this paper we report the discovery, confirmation and characterisation of MASCARA-3[2], the fourth planetary system found through the MASCARA survey. MASCARA-3b is a hot Jupiter with a 5.6 day period, and orbits a bright late F-type star ($V = 8.33$). In Sec. 2 the discovery observations from MASCARA and the spectroscopic follow-up observations with SONG (Stellar Observation Network Group, Andersen et al. 2014) are described. The analysis and results of the host star are presented in Sec. 3, while Sec. 4 contains the investigation and characterisation of its planet. The results are presented and discussed in Sec. 5.

2. Observations

In this section two different kinds of observations are presented: the MASCARA photometry and the SONG spectroscopy (see Table 1).

⋆ hjorth@phys.au.dk
[1] `http://exoplanet.eu`
[2] During the final preparations for this paper, we learned of the publication of the discovery of the same planetary system by the KELT-team; KELT-24 (**?**)

MASCARA : The MASCARA survey is described in Talens et al. (2017b). In short, it consists of two instruments: one covering the northern sky at the Observatory del Roque de los Muchachos (La Palma, Spain) and one targeting the southern hemisphere located at the European Southern Observatory (La Silla, Chile). Each instrument consists of five wide-field CCD's, which record images of the local sky throughout the night employing 6.4 sec exposure times. Aperture astrometry is performed on all known stars brighter than $V = 8.4$. The light curves are extracted from the raw flux following the procedure described in Talens et al. (2018a), and transit events are searched for using the Box Least-Square (BLS) algorithm of Kovács et al. (2002). MASCARA-3 has been monitored since early 2015 by the northern instrument, totalling more than 27247 calibrated photometric data points, each consisting of 50 binned 6.4 second measurements (i.e. 320 sec per data point). A frequency analysis was performed on the light curve measurements by computing its BLS periodogram, revealing a peak at a period of 5.55149 days. Phasefolding the light curve using this period, we performed a preliminary analysis on the system, obtaining parameter values useful for spectroscopic follow-up (see Table 2). The resulting phasefolded lightcurve is shown in Fig. 1.

SONG : Succeeding the transit detection in the light curve of MASCARA-3, follow-up spectroscopy was executed using the 1 meter Hertzsprung SONG telescope (Andersen et al. 2014) at Observatory del Teide (Tenerife, Spain). The observations were done in order to validate and characterise the planetary system. The telescope is equipped with a high-dispersion echelle spectrograph which covers the wavelength range 4400 – 6900Å. A total of 92 spectra were obtained between April 2018 and April 2019, employing a slit width of 1.2 arcsec resulting in a resolution of $R \sim 77,000$. The exposure times had been varied between 600 and 1800 sec. We used longer exposure times out of transits and shorter exposure times during transits to reduce phase smearing. 45 of the observations were gathered during two planetary transits occuring on May 29, 2018 and November 28, 2018. For the first transit our spectroscopic observations cover the entire transit. However, due to bad weather only a single spectrum was taken out of transit. On the second night we obtained a partial transit and post egress spectra.

As we analyze the RM effect in this system using the Doppler Tomography technique we did not use an iodine cell for observations taken during transit nights, but sandwiched each observation with ThAr exposures for wavelength calibration. From these spectra we obtained cross-correlation functions (CCFs) and Broadening Functions (BFs) Rucinski (2002). Spectra not taken during transit nights were obtained with an iodine cell inserted into the light path.

The spectra and radial velocity (RV) extraction was performed following Grundahl et al. (2017). The RV data points are estimated to have internal instrumental uncertainties of $\sim$ 31 m sec^{-1}. The resulting RVs and their uncertainties are listed in Table A.1.

3. Stellar characterisation

We determined the spectroscopic effective temperature $T_{\rm eff} = 6415 \pm 110$ K and metallicity [Fe/H] $= 0.09 \pm 0.09$ dex using `SpecMatch-emp` (Yee et al. 2017), classifying it as an F7 star. `SpecMatch-emp` compares the observed spectrum with an empirical spectral library of well-characterised stars. Using the BAyesian STellar Algorithm `BASTA` (Silva Aguirre et al. 2015) with a grid of BaSTI isochrones (Pietrinferni et al. 2004; Hidalgo et al. 2018), we combined the spectroscopically derived $T_{\rm eff}$ and [Fe/H] with the 2MASS JHK magnitudes (see Table 3) and *Gaia* DR2 parallax ($\pi = 10.33 \pm 0.11$ mas) to obtain a final set of stellar parameters. Given the proximity of the star we assumed zero extinction along the line of sight. This way we derived a stellar mass $M_\star = 1.30^{+0.04}_{-0.03} M_\odot$, radius $R_\star = 1.52^{+0.03}_{-0.02} R_\odot$, and stellar age $= 2.8^{+0.5}_{-0.6}$ Gyr.

Table 1. Observation log of MASCARA-3 containing the different types of observation, instrument, no. of observations made and observing dates.

Type	Inst.	No. of obs.	Obs. date
Phot.	MASCARA	27247	February 2015 – March 2018
RV Spec.	SONG	47	April 2018 – April 2019
RM Spec.	SONG	23	29 May 2018
RM Spec.	SONG	22	28 November 2018

Table 2. Best fit values for the *initial* analysis of the MASCARA photometric data, with the eccentricity kept fixed at 0. Of these parameters, P and T_0 were used as priors in the joint fit between the spectroscopy and phasefolded photometry.

Parameter	Value
Orbital period, P (days)	5.55149±0.00002
Time of mid-transit, T_0 (BJD)	$2458268.455^{+0.002}_{-0.003}$
Total transit duration, T_{14} (hr)	4.3±0.1
Scaled planetary radius, $R_{\rm p}/R_\star$	0.091±0.002
Scaled orbital distance, $a/R_\star$	$10.4^{+0.4}_{-1.0}$
Orbital inclination, i (deg)	88±1.0
Impact parameter, b	0.3±0.2

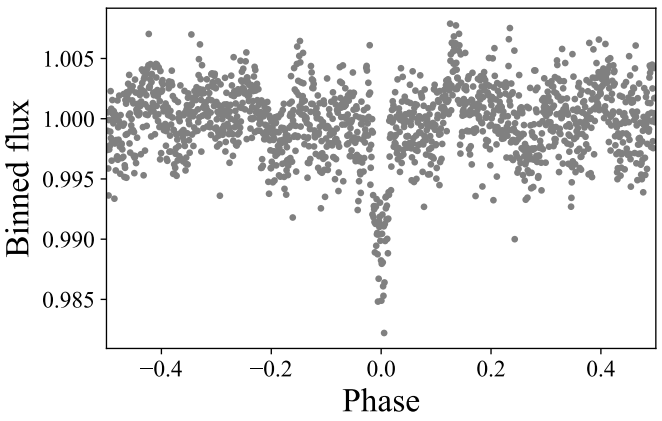

Fig. 1. Calibrated and phasefolded MASCARA-3 photometry. The phase-folded data have been binned to 5 min. intervals, reducing the number of data points from 27247 to 1596. The period of 5.55149 days used in the phasefolding is the highest peak obtained from constructing the BLS periodogram of the data.

4. Photometric and spectrocopic analysis

The overall analysis of the photometry and RV data is done in a similar fashion as for MASCARA-1b (Talens et al. 2017a) and

Table 3. Literature and best-fit parameters for the stellar analysis of MASCARA-3. Sources: *Extracted from *Gaia* DR2 (Gaia Collaboration et al. 2018, `https://gea.esac.esa.int/archive/`). †Parameters from 2MASS (Cutri et al. 2003). ‡From the Tycho catalogue (Høg et al. 2000). The remaining parameter values are from this work.

Parameter	Value
Identifiers	HD 93148
Spectral type	F7
Right ascension, α (J2000.0)*	$10^{\rm h}\ 47^{\rm m}\ 38.351^{\rm s}$
Declination, δ (J2000.0)*	$+71^\circ\ 39'\ 21.16''$
Parallax, π (mas)*	10.3±0.1
Distance (pc)*	97±1
V-band mag., $V^\dagger$	8.33±0.01
J-band mag., $J^\ddagger$	7.41±0.02
H-band mag., $H^\ddagger$	7.20±0.04
K-band mag., $K^\ddagger$	7.15±0.02
Effective temperature, $T_{\rm eff,\star}$ (K)	6415 ± 110
Surface gravity $\log {\rm g}_\star$ (cgs)	$4.18^{+0.01}_{-0.02}$
Metallicity, [Fe/H] (dex)	0.09 ± 0.09
Age (Gyr)	$2.8^{+0.5}_{-0.6}$
Stellar mass, $M_\star$ ($M_\odot$)	$1.30^{+0.04}_{-0.03}$
Stellar radius, $R_\star$ ($R_\odot$)	$1.52^{+0.03}_{-0.02}$
Stellar density, $\rho_\star$ (g cm^{-3})	$0.52^{+0.04}_{-0.03}$

MASCARA-2b (Talens et al. 2018b) and is outlined in the following section. Given the transit phase coverage and low Signal-to-Noise Ratio (SNR) of the RM detection we modified our analysis for that this data set accordingly. We give details on that in sections 4.2.1 and 4.2.2.

4.1. Joint photometric and RV analysis

The binned, phasefolded MASCARA light curve is modelled employing the model by Mandel & Agol (2002), using a quadratic limb-darkening law. The free parameters for the transit model are the orbital period (P), a particular mid-transit time (T_0), the semi-major axis scaled by the stellar radius ($a/R_\star$), the scaled planetary radius ($R_p/R_\star$), the orbital inclination (i), the eccentricity (e) and the argument of periastron (ω) and finally the quadratic limb-darkening parameters (c_1) and (c_2). For efficiency, the inclination, eccentricity and argument of periastron are parameterized through $\cos i$, $\sqrt{e}\cos\omega$ and $\sqrt{e}\sin\omega$.

For the modelling of the RV observations, we only use spectra obtained with an iodine cell insert in the light path (Table A.1). This excludes data taken during transit nights. The RV data is compared to a Keplerian model where the stellar RV variations are caused by the transiting object. The additional parameters needed to describe the RV data are the RV semi-amplitude (K) and a linear offset in RV (γ). In addition, we allow for a linear drift of the RV data points, $\dot{\gamma}$, caused by e.g. a long-period unseen companion.

To characterise the planetary system we jointly model the the light curve and the RVs. Since we fit to the *phasefolded* light curve, we impose Gaussian priors $P = 5.55149 \pm 0.00002$ days and $T_0 = 2458268.455^{+0.002}_{-0.003}$ BJD retrieved from the photometric analysis described in Section 2. In addition we impose Gaussian priors of $c_1 = 0.3797$ and $c_2 = 0.2998$ (Claret & Bloemen 2011; Eastman et al. 2013) with a conservative uncertainties of 0.1. Furthermore, by using the spectroscopic value of the density $\rho_\star = 0.52^{+0.04}_{-0.03}$ g cm^{-3} as a prior, we can constrain the orbital shape and orientation (see e.g. Van Eylen & Albrecht 2015, and references therein).

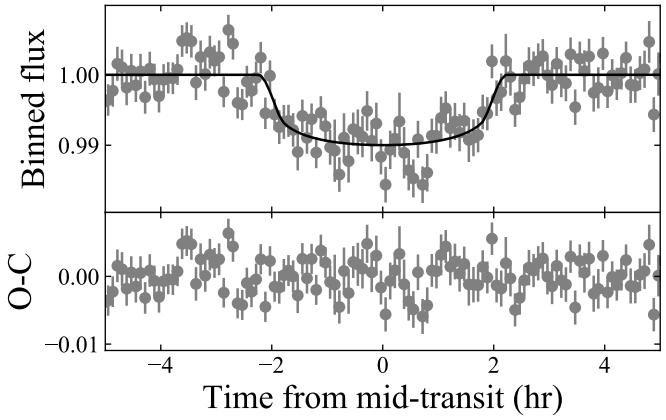

Fig. 2. The phasefolded MASCARA-3 photometry data (grey) with the best-fit transit model (black) from the joint photometric and RV analysis. The corresponding best-fit parameters can be found in Table 4. The bottom plot displays the residuals.

The log-likelihood for each data set is given as

$$\ln \mathcal{L} = -\frac{1}{2}\sum_{i=1}^{N}\left(\ln\left(2\pi\left[\sigma_i^2+\sigma_{\rm jit}^2\right]\right)+\frac{[O_i-C_i]^2}{\left[\sigma_i^2+\sigma_{\rm jit}^2\right]}\right) \quad (1)$$

with O_i and C_i being the i'th of N data and model points in each data set. For the two data sets we introduce two jitter terms $\sigma_{\rm jit,p}$ and $\sigma_{\rm jit,RV}$ to capture any unaccounted noise. These jitter terms are added in quadrature to the internal errors σ_i when calculating the maximum likelihood. The total log-likelihood is the sum of eq. 1 for the photometry and RV together with an additional likelihood term accounting for priors.

The posterior distribution of the parameters are sampled through `emcee`, an MCMC multi-walker Python package (Foreman-Mackey et al. 2013). We initialize 200 walkers close to the maximum likelihood. They are evaluated for 10 000 steps, with a burn-in of 5000 steps which we disregard. By visually inspecting trace plots we have checked that the solutions have converged at that point. In Table 4 we report the maximum likelihood values of the MCMC sampling. The quoted uncertainty intervals represent the range that excludes 15.85% of the values on each side of the posterior distribution and encompass 68.3% of the probability. Fig. 2 and 3 displays the data and best-fit models for the joint analysis of the light curve and the RVs.

4.2. Analyzing the stellar absorption line

Modelling the stellar absorption lines is carried out in a similar way as was done in Albrecht et al. (2007) and Albrecht et al. (2013). However we modified our approach of comparing the model to the data. We did this because we found that BFs created from our data had a too low SNR to be useful in determining λ through analysis of the RM effect. Nevertheless they more faithfully represent the width of the stellar absorption lines than the CCFs which have large "wings"(See fig. 4). We have not been able to determine the exact underlying reason for this, but we suspect that the low SNR in the spectra is to blame. Determining the correct continuum level in low SNR high resolution spectra is extremely difficult. For the case of MASCARA-3, this problem is enlarged due to the fast stellar rotation and therefore wide

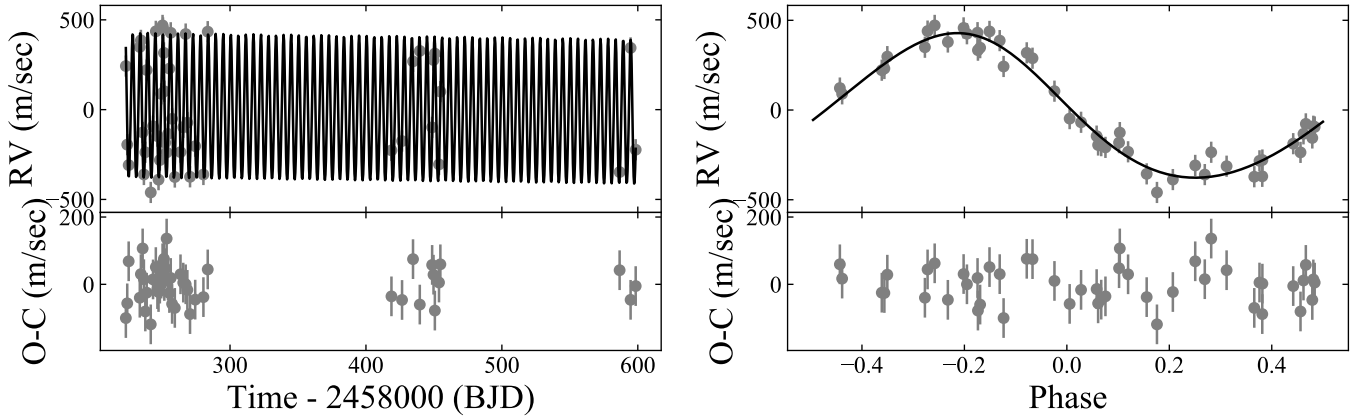

Fig. 3. The RV data from the SONG telescope (grey) with the best-fit keplerian model (black) from the joint photometric and RV analysis. The data is plotted as a function of time (left) and phasefolded (right), to highlight the fact that we allowed for the possibility of a linear trend in the RV. In the panel on the right side the best fitting RV trend was removed from the data and model. The best-fit parameters are displayed in Table 4. The bottom plot shows the residuals.

Table 4. The best-fitting and derived stellar, planetary and system parameters for MASCARA-3. The parameters are extracted from the joint analysis on the photometry and RV (Sec. 4.1), the analysis on the mean out of transit BF (Sec. 4.2.1) and the analysis on the contour of the shifted and binned Doppler shadow residuals (Sec. 4.2.2).

Parameter	Value	Section
Fitting parameters		
Quadratic limb darkening (MASCARA), (c_1, c_2)	$(0.40 \pm 0.07, 0.31 \pm 0.07)$	4.1
Systemic velocity, γ (km s^{-1})	-5.62 ± 0.01	4.1
Linear trend in RV, $\dot{\gamma}$ (m s^{-1} yr^{-1})	-0.037 ± 0.029	4.1
Orbital period, P (days)	5.55149 ± 0.00001	4.1
Time of mid-transit, T_0 (BJD)	2458268.455 ± 0.002	4.1
Scaled planetary radius, $R_p/R_\star$	$0.091^{+0.002}_{-0.003}$	4.1
Scaled orbital distance, $a/R_\star$	9.5 ± 0.16	4.1
RV semi-amplitude, $K_\star$ (m s^{-1})	403 ± 12	4.1
$\sqrt{e}\sin\omega$	$0.19^{+0.07}_{-0.10}$	4.1
$\sqrt{e}\cos\omega$	0.21 ± 0.04	4.1
$\cos i$	$0.034^{+0.012}_{0.018}$	4.1
Jitter term phot., $\sigma_{\rm jit,p}$	0.0021 ± 0.0001	4.1
Jitter term RV, $\sigma_{\rm jit,RV}$ (km s^{-1})	0.050 ± 0.08	4.1
Quadratic limb darkening (SONG), ($c_{1,s}$, $c_{2,s}$)	$(0.66 \pm 0.09, 0.40 \pm 0.09)$	4.2.1
Microturbulence, β (km s^{-1})	4.3 ± 0.6	4.2.1
Macroturbulence, ζ (km s^{-1})	9.4 ± 0.4	4.2.1
Proj. rotation speed BF, $v \sin i_\star$ (km s^{-1})	20.4 ± 0.4	4.2.2
Jitter term RM out of transit, $\sigma_{\rm jit,out}$ (m s^{-1})	0.003 ± 0.002	4.2.1
Proj. rotation speed contour, $v \sin i_\star$ (km s^{-1})	20.3 ± 8.1	4.2.2
Projected obliquity, λ (deg)	10.5 ± 24.9	4.2.2
Contour rotation θ (deg)	-4.0	4.2.2
Contour offset f	0.295	4.2.2
Contour scaling h	0.21	4.2.2
Derived parameters		
Orbital eccentricity, e	$0.085^{+0.023}_{-0.022}$	
Argument of periastron, ω (deg)	41^{+14}_{-20}	
Orbital inclination, i (deg)	$88.1^{+1.0}_{-0.7}$	
Impact parameter, b	0.32 ± 0.01	
Total transit duration, T_{14} (hr)	4.68 ± 0.09	
Full transit duration, T_{23} (hr)	3.81 ± 0.07	
Semi-major axis, a (au)	0.067 ± 0.002	
Planetary mass, M_p ($M_{\rm Jup}$)	4.2 ± 0.2	
Planetary radius, R_p ($R_{\rm Jup}$)	1.35 ± 0.05	
Planetary mean density, ρ_p (g cm^{-3})	2.3 ± 0.3	
Equilibrium temperature, $T_{\rm eq}$ (K)	1473 ± 28	

stellar absorption lines. A mismatch in the continuum would lead to a low SNR in the derived BF. The same mismatch in the continuum correction would lead to enlarged "wings" in the CCFs. We therefore first obtained a measure for $v \sin i_\star$ by comparing our out of transit stellar line model to an average out of transit BF. We then analyze the "planet shadow" in the transit data.

Concerning the model for comparison to the out of transit and in transit data we did the following: We created a 201×201 grid containing a pixelated model of the stellar disk. The brightness of each pixel on the stellar disk is scaled according to a quadratic limb-darkening law with the parameters $c_{1,s}$ and $c_{2,s}$ and set to zero outside the stellar disk. Each pixel is also assigned a radial velocity assuming solid body rotation and a particular projected stellar rotation speed, $v \sin i_\star$. The RVs of each pixel are further modified following the model for turbulent stellar motion as described in Gray (2005). This model has two terms. A micro-turbulence term modelled by a convolution with a Gaussian, which σ-width we describe here with the parameter β. The second term in this model encompasses radial and tangential macro turbulence surface motion. Its σ-width we assign the parameter ζ. The modelled stellar absorption line is then obtained by disk integration. Finally the Gaussian convolution also includes the Point Spread Function (PSF) of the spectrograph added in quadrature. Because of the low SNR of our spectra we do not include convective blueshift in our model.

4.2.1. Out of transit stellar absorption line

To measure $v \sin i_\star$ we compared our out of transit line model to the BFs taken out of transit. We used only data from the second transit night as little data was obtained out of transit during the first transit night (Fig. 5). In addition to the five model parameters, $c_{1,s}$, $c_{2,s}$, $v \sin i_\star$, β, and ζ, we also vary a jitter term $\sigma_{\rm jit,out}$ during the fitting routine. We impose Gaussian priors of $\beta = 2.7$ km sec^{-1} (Coelho et al. 2005) and $\zeta = 6.1$ km sec^{-1} (Gray 1984), both with uncertainty widths of 0.5 km sec^{-1}. The best-fit parameters are again found by maximizing the log-likelihood from eq. 1 using `emcee` in the same way as in Sec. 4.1. The best-fit parameters are given in Table 4, while the data and best-fit model are shown in Fig. 4.

4.2.2. The Doppler shadow

We observed spectroscopic transits during the nights 29-5-2018 and 28-11-2018. This was done, in order to validate the companion being a planet orbiting the host star and to obtain the projected spin-orbit angle (or projected obliquity, λ) of the system.

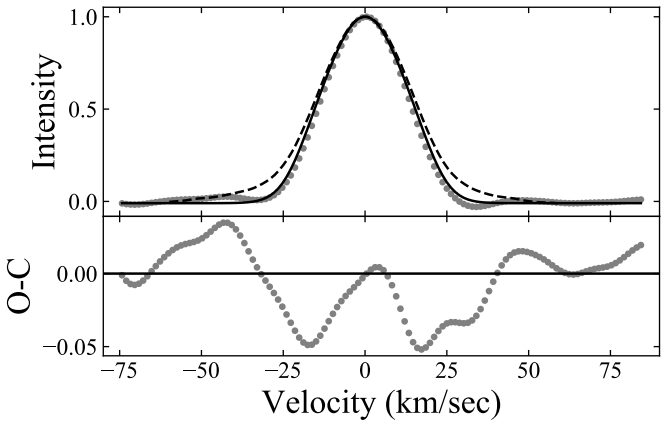

Fig. 4. The mean out of transit BF (grey) with the best fitting stellar absorption line model (black). For comparison the dashed line shows the mean out of transit CCF, which erroneously leads to an enlarged line-width due to its "wings", which we assume are caused by a none perfect normalization of the low SNR spectra, see text.

During transit, the planet will block some of the star, deforming the absorption line by reducing the amount of blue- or redshifted light visible to the observer at a particular phase of a transit. Subtracting the distorted in-transit absorption lines to the out of transit line will therefore reveal the planetary "shadow" cast onto the rotating stellar photosphere. For solid body rotation this shadow travels on a line in a time-velocity diagram and its zero point in velocity and orientation depends on the projected obliquity and projected stellar rotation speed, as well as the impact parameter. See eq. 4 in **?**. The planet shadows obtained during the two transit nights can be seen in Fig. 5. Here we have removed the average out of transit CCF from the second transit night from all observations. Clearly MASCARA-3 b travels on a prograde orbit. During the first half of the transit the distortion has negative RVs ,and positive RVs during the second half of the transit. However as our detection of the planet shadow is of low SNR we do not strictly follow Albrecht et al. (2013) and Talens et al. (2017a) in deriving λ. Rather we use an approach similar to the one pioneered by Johnson et al. (2014).

In this method, a dense grid of $v \sin i_\star$ and λ values is created. For each of these ($v \sin i_\star$, λ) pairs, we compute the RV rest frame of the sub planetary point. For each observation the data is then shifted into this RV rest frame of the sub planetary point. Subsequently the observations are collapsed and the signal from both nights is co-added. The closer the values for λ and $v \sin i_\star$ in the grid are to the actual values of these parameters, the more significant the peak will be. We display a contour plot of these peak values in Fig. 6.

To obtain the best-fit parameters for $v \sin i_\star$ and λ, we now fit a 2D Gaussian to the grid of peak values we have just obtained. For this 2D Gaussian fit we use, next to $v \sin i_\star$ and λ, the width of the Gaussian in each direction $\sigma_{v \sin i_\star}$ and σ_λ, and the following nuisance parameter: a rotation angle θ, a scaling parameter h and an offset parameter f. This way we obtain $v \sin i_\star$ = 20.3 ± 8.1 km sec^{-1} and λ = 10.5 ± 24.9°. While we take this λ = 10.5 ± 24.9° value as our final result we do prefer the $v \sin i_\star$ value obtained from the fit to the out of transit BF as our final value for the projected stellar rotation speed. These are the values reported in Table 4.

5. Discussion and Conclusions

From the joint photometry and RV analysis we obtain a planetary mass of $4.2 \pm 0.2\ M_{\rm Jup}$ and a planetary radius of $1.35 \pm 0.05\ R_{\rm Jup}$. The planet revolves around its host star on an almost circular orbit ($e = 0.085^{+0.023}_{-0.022}$) every 5.55149 ± 0.00001 days at a distance of 0.067 ± 0.002 au, making MASCARA-3b a hot Jupiter. With an incident flux of $F = (10.6 \pm 0.9) \cdot 10^8$ erg s^{-1} cm^{-2} above the inflation threshold of $F = 2 \cdot 10^8$ erg s^{-1} cm^{-2} (Demory & Seager 2011), the planet might be affected by inflation mechanisms, despite having a mean density above that of Jupiter.

It is still unclear whether hot Jupiters primarily originate from High Eccentricity Migration (HEM) or disk migration (for a review, see Dawson & Johnson 2018). The former process would lead to at least occasionally large obliquities while the latter process would lead to low obliquities, assuming good alignment between stellar spin and angular momentum of the protoplanetary disks, but see also **?**. However the interpretation of hot Jupiter obliquities might be more complicated than originally thought. This is because tidal interactions might have aligned the stellar spin and the orbital angular momentum in some of the systems, in particular in systems where the host stars have a convective envelope, leading to fast alignment of the planets orbital spin with the stellar rotation Winn et al. (2010); Albrecht et al. (2012).

With an effective temperature of $T_{\rm eff,\star}$ = 6415 ± 110 K, MASCARA-3 will have a relatively slow alignment timescale for a hot Jupiter of its mass and distance. It is also interesting to note that the orbital eccentricity suggests a near circular orbit. MASCARA-3 b appears to belong to a dynamically cold population consistent with an arrival at its current orbit via disk migration instead of HEM. Consistent with this picture is that we have not fund a long term RV trend which would indicate the presence of a third body in the system, that could have initiated HEM migrations via a scatter event or secular dynamics, like Kozai-Lidov cycles. However the time line of our observations is to short to exclude such a body.

While finalizing the manuscript we learned of another paper reporting the discovery of this planet-star system published by the KELT team. Though no observations or analyses were shared, the planet and system parameters from our papers are for the most part in agreement. The only major difference is the RV semi-amplitude, and thereby the derived planetary mass.

Acknowledgements. We would like to thank Anaël Wünsche, Marc Bretton, Raoul Behrend, Patrice Le Guen, Stéphane Ferratfiat, Pierre Dubreuil and Alexandre Santerne for their effort in obtaining ground-based follow-up photometry during transit. MH, SA and ABJ acknowledge support by the Danish Council for Independent Research, through a DFF Sapere Aude Starting Grant nr. 4181-00487B, and the Stellar Astrophysics Centre which funding is provided by The Danish National Research Foundation (Grant agreement no.: DNRF106). IAGS acknowledges support from a NWO VICI grant (639.043.107). EP acknowledges support from Spanish MINECO grant (ESP2016-80435-C2-2-R).This project has received funding from the European Research Council (ERC) under the European Union's Horizon 2020 research and innovation programme (grant agreement nr. 694513). Based on observations made with the Hertzsprung SONG telescope operated on the island of Tenerife by the Aarhus and Copenhagen Universities in the Spanish Observatorio del Teide of the Instituto de Astrofísica de Canarias. The Hertzsprung SONG telescope is funded by the Danish National Research Foundation, Villum Foundation, and Carlsberg Foundation. This work uses results from the European Space Agency (ESA) space mission Gaia. Gaia data are being processed by the Gaia Data Processing and Analysis Consortium (DPAC). Funding for the DPAC is provided by national institutions, in particular the institutions participating in the Gaia MultiLateral Agreement (MLA). The Gaia mission website is `https://cosmos.esa.int/gaia`. The Gaia archive website is `https://archives.esac.esa.int/gaia`.

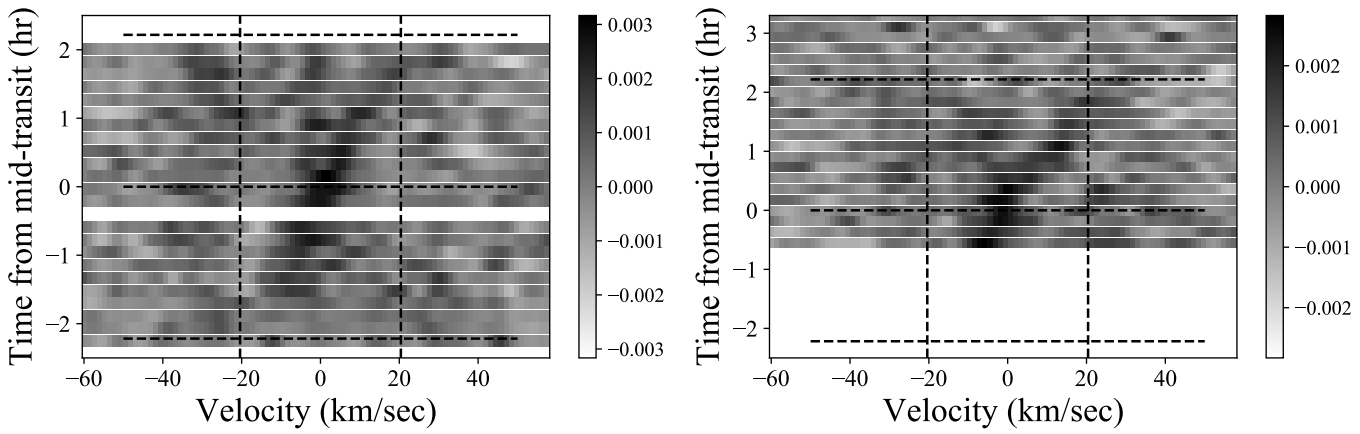

Fig. 5. The spectroscopic transit of MASCARA-3 observed on the night of 29-05-2018 (left) and 28-11-2018 (right). Both plots show the observed CCFs, with the subtraction of the mean out of transit CCF obtained from the second night. Before subtraction, these CCFs are scaled and offset to their model-counterpart in intensity (all CCFs) and scaled in velocity-space (in-transit CCFs), in order to account for uneven normalisation due to differences in flux-levels and PSF changes. The vertical dashed lines mark the best-fit value of the $v \sin i_\star$ from the BF analysis, while the horizontal dashed lines mark the best-fit value for the transit ingress, mid-transit time and egress.

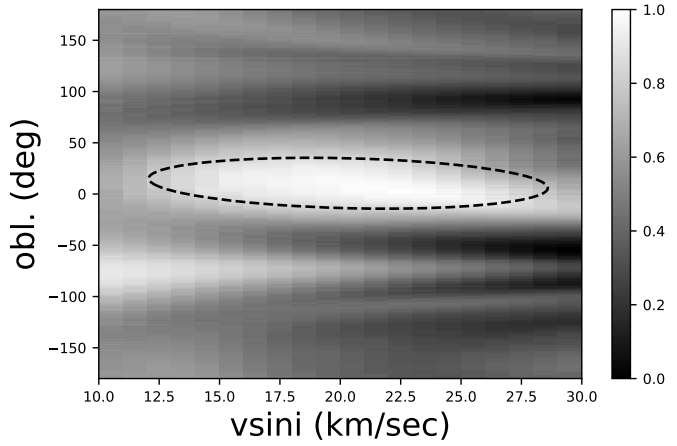

Fig. 6. The enhancement ($v \sin i_\star$, λ) grid together with the best-fit 1σ 2D Gaussian model (dashed). For each ($v \sin i_\star$, λ) pair the grid values are constructed by shifting the model and shadow bump a corresponding amount, such that the model shadow bump is centered at zero. This is followed by collapsing the shifted data shadow in intensity space. The contour signal at a specific ($v \sin i_\star$, λ) value is then the resulting value of the collapsed, shifted data shadow at a velocity of zero.

References

Albrecht, S., Reffert, S., Snellen, I., Quirrenbach, A., & Mitchell, D. S. 2007, A&A, 474, 565
Albrecht, S., Winn, J. N., Johnson, J. A., et al. 2012, ApJ, 757, 18
Albrecht, S., Winn, J. N., Marcy, G. W., et al. 2013, ApJ, 771, 11
Andersen, M. F., Grundahl, F., Christensen-Dalsgaard, J., et al. 2014, in Revista Mexicana de Astronomia y Astrofisica Conference Series, Vol. 45, Revista Mexicana de Astronomia y Astrofisica Conference Series, 83–86
Bakos, G., Noyes, R. W., Kovács, G., et al. 2004, PASP, 116, 266
Barge, P., Baglin, A., Auvergne, M., et al. 2008, A&A, 482, L17
Borucki, W. J., Koch, D., Basri, G., et al. 2010, Science, 327, 977
Claret, A. & Bloemen, S. 2011, A&A, 529, A75
Coelho, P., Barbuy, B., Meléndez, J., Schiavon, R. P., & Castilho, B. V. 2005, A&A, 443, 735
Collier Cameron, A., Bruce, V. A., Miller, G. R. M., Triaud, A. H. M. J., & Queloz, D. 2010, MNRAS, 403, 151
Cutri, R. M., Skrutskie, M. F., van Dyk, S., et al. 2003, VizieR Online Data Catalog, 2246
Dawson, R. I. & Johnson, J. A. 2018, ArXiv e-prints [arXiv:1801.06117]
Demory, B.-O. & Seager, S. 2011, ApJS, 197, 12
Dorval, P., Talens, G. J. J., Otten, G. P. P. L., et al. 2019, arXiv e-prints [arXiv:1904.02733]
Eastman, J., Gaudi, B. S., & Agol, E. 2013, PASP, 125, 83
Foreman-Mackey, D., Hogg, D. W., Lang, D., & Goodman, J. 2013, PASP, 125, 306
Gaia Collaboration, Brown, A. G. A., Vallenari, A., et al. 2018, ArXiv e-prints [arXiv:1804.09365]
Gray, D. 2005, The Observation and Analysis of Stellar Photospheres (Cambridge University Press)
Gray, D. F. 1984, ApJ, 281, 719
Grundahl, F., Fredslund Andersen, M., Christensen-Dalsgaard, J., et al. 2017, ApJ, 836, 142
Hidalgo, S. L., Pietrinferni, A., Cassisi, S., et al. 2018, ApJ, 856, 125
Høg, E., Fabricius, C., Makarov, V. V., et al. 2000, A&A, 355, L27
Howell, S. B., Sobeck, C., Haas, M., et al. 2014, PASP, 126, 398
Johnson, M. C., Cochran, W. D., Albrecht, S., et al. 2014, ApJ, 790, 30
Kovács, G., Zucker, S., & Mazeh, T. 2002, A&A, 391, 369
Lund, M. B., Rodriguez, J. E., Zhou, G., et al. 2017, AJ, 154, 194
Mandel, K. & Agol, E. 2002, ApJ, 580, L171
Pepper, J., Pogge, R. W., DePoy, D. L., et al. 2007, PASP, 119, 923
Pietrinferni, A., Cassisi, S., Salaris, M., & Castelli, F. 2004, ApJ, 612, 168
Pollacco, D. L., Skillen, I., Collier Cameron, A., et al. 2006, PASP, 118, 1407
Ricker, G. R., Winn, J. N., Vanderspek, R., et al. 2015, Journal of Astronomical Telescopes, Instruments, and Systems, 1, 014003
Rucinski, S. M. 2002, AJ, 124, 1746
Rucinski, S. M. 2004, in Stellar Rotation, Vol. 215, 17
Silva Aguirre, V., Davies, G. R., Basu, S., et al. 2015, MNRAS, 452, 2127
Snellen, I. A. G., de Kok, R. J., de Mooij, E. J. W., & Albrecht, S. 2010, Nature, 465, 1049
Talens, G. J. J., Albrecht, S., Spronck, J. F. P., et al. 2017a, A&A, 606, A73
Talens, G. J. J., Deul, E. R., Stuik, R., et al. 2018a, ArXiv e-prints [arXiv:1810.04060]
Talens, G. J. J., Justesen, A. B., Albrecht, S., et al. 2018b, A&A, 612, A57
Talens, G. J. J., Spronck, J. F. P., Lesage, A.-L., et al. 2017b, A&A, 601, A11
Van Eylen, V. & Albrecht, S. 2015, ApJ, 808, 126
Winn, J. N., Fabrycky, D., Albrecht, S., & Johnson, J. A. 2010, ApJ, 718, L145
Yee, S. W., Petigura, E. A., & von Braun, K. 2017, ApJ, 836, 77

Appendix A: Extra material

Table A.1. Radial velocities at different times for MASCARA-3 using the SONG telescope. We list the barycentric time of mid-exposure and the RVs corrected for barycentric motion. All spectra were taken with the iodine cell as reference. The instrumental uncertainty (σ_{RV}) is estimated to be 31.1 m sec^{-1}. However the data appears to present an additional jitter term (see Table 4).

Time (BJD)	RV+6000 (m s^{-1})
2458223.357685	621.2
2458224.382018	183.5
2458225.434460	69.6
2458233.607846	727.4
2458234.418452	764.2
2458235.720058	251.5
2458236.641036	17.4
2458237.678446	141.1
2458238.692052	598.9
2458241.674223	-82.6
2458243.368995	286.2
2458245.410918	814.5
2458246.571993	230.8
2458247.398019	-11.4
2458248.368253	97.5
2458249.365280	466.3
2458250.368275	847.5
2458250.681785	833.6
2458251.366037	694.6
2458251.666389	480.9
2458252.366480	194.1
2458253.365122	140.3
2458254.365100	242.9
2458255.374490	606.8
2458256.384282	806.4
2458257.382395	327.3
2458259.383303	3.4
2458263.567251	141.9
2458265.589542	280.1
2458267.372280	799.4
2458268.609046	305.9
2458270.572919	4.5
2458274.379165	175.1
2458280.423224	17.4
2458283.600292	812.6
2458418.763646	151.7
2458426.556824	203.5
2458434.627715	647.1
2458439.611331	705.5
2458448.692687	279.8
2458449.708606	654.5
2458450.690659	690.4
2458453.742034	73.5
2458454.745732	478.9
2458586.621310	30.9
2458594.703421	722.2
2458598.446201	155.2